International Communications in Heat and Mass Transfer 113 (2020) 104518

Contents lists available at ScienceDirect

International Communications in Heat and Mass Transfer

journal homepage: www.elsevier.com/locate/ichmt

Buoyancy-driven instabilities and particle deposition in a Taylor-Couette apparatus

Mohamed Aksouh[a,*], Rachida Chemini[b], Amina Mataoui[a], Sébastien Poncet[c]

[a] Faculty of Physics, USTHB, Algiers, Algeria
[b] Faculty of Mechanical and Process Engineering, USTHB, Algiers, Algeria
[c] Mechanical Engineering Department, Université de Sherbrooke, Sherbrooke, QC, Canada

ARTICLE INFO

Keywords:
Taylor-Couette flow
Natural convection
Buoyancy-driven instability
Lagrangian particle tracking
Numerical simulation

ABSTRACT

The present paper aims at studying the particle trajectories and sedimentation inside Taylor-Couette buoyancy-driven flows. The dynamical and thermal features of Taylor–Couette-flows inside a three-dimensional differentially heated cavity are investigated for Reynolds numbers Re ranging from 67.3 to 392.7 and Grashof numbers Gr between $764.4 \leq Gr \leq 3822.1$. The results indicate a strong interaction between natural convection and the base Taylor-Couette flow due to rotation for a weak radial temperature gradient. A spectral analysis allows to identify different flow regimes. For discrete particle simulations, the Lagrangian Particle Tracking method is used to follow the particle trajectories inside the Taylor-Couette apparatus. Water droplets are considered as solid spherical particles with different diameters ($10 \leq D_p \leq 35$ μm). The time analysis of suspended and deposited particles along different walls shows that the rotation of the inner-cylinder coupled to the natural convection influences significantly the time and location of the particle deposition.

1. Introduction

A viscous fluid confined in an annular space of two rotating coaxial cylinders is called Taylor–Couette flow. The Taylor-Couette configuration is characterized by height-to-gap aspect ratio $\Gamma = H/(r_o - r_i)$ and the radius-ratio $\eta = r_i/r_O$. For ideal case, the height-to-gap aspect ratio tends to infinity ($\Gamma \to \infty$) and the radius ratio is equal to unity ($\eta = 1$). However, for rotating machinery, such as rotating compressors, turbomachines, electrical motors, rotating heat exchangers, the height of the cylinders is finite inducing thus end-wall effects on the flow structure. As an example, Lalaoua and Naït Bouda [1] recently performed a numerical investigation on the onset of axisymmetric and wavy Taylor-Couette flows between three combinations of cylinders and spherocylinders, which modify the end-cap conditions of the classical Taylor-Couette configuration. Their results showed that the transition from one regime to another is delayed compared to the base case between concentric cylinders.

Similarly, imposing a radial temperature gradient between the two cylinders engenders an axial flow due to natural convection. Since many decades, several studies were performed experimentally [2–4], theoretically [5,6] and numerically [7,8]. These studies were carried out to understand the stability and flow structures for combined Taylor-Couette and natural convection flow. Apart from being a canonical flow to understand the route to turbulence, Taylor-Couette flows are also relevant in many industrial applications: chemical vapor deposition techniques, crystal growth, cooling of rotating electrical motors, reactor fuel rods and rotating tube heat exchangers [9], among other examples.

By heating the rotating inner cylinder and keeping the outer cylinder stationary (RHISCO), the buoyancy effects modify significantly the Taylor vortices which are altered inside the annular space [7]. The same flow behavior was detected experimentally by Lepiller et al. [4] on the stability of Taylor-Couette flow subjected to a weak radial temperature gradient. They found that the radial temperature gradient destabilizes the Taylor-Couette flow leading to a pattern of moving helical vortices only near the bottom below the threshold of the Taylor vortices. The size of the pattern increases as the rotation frequency of the cylinder raises. However, Sorour and Coney [3] showed experimentally that the stability curve is independent of fluid properties, but varies versus the annular radius-ratio, Taylor number and temperature difference. In a tall Taylor-Couette apparatus ($\Gamma = 80$ and $\eta = 0.8$), the formation of instabilities was investigated numerically by Viazzo and Poncet [10]. Seven instability regimes were highlighted by DNS calculations as spiral rolls being regular (SPI), modulated (MSPI), wavy (WSPI) or with defects (SPI + D), Taylor vortex flow (TVF) or wavy vortex flow (WVF) or a combination of both (SPI + WVF), confirming the experimental results of Guillerm [11]. In a recent work, Lopez et al.

* Corresponding author.
E-mail address: maksouh@usthb.dz (M. Aksouh).

https://doi.org/10.1016/j.icheatmasstransfer.2020.104518

Nomenclature

Latin symbols

C	Particle concentration
C_D	Drag coefficient
d	Gap size (m)
D_P	Particle diameter (m)
f_i	Rotation frequency of inner cylinder
F_D	Drag force (N)
g	Acceleration due to gravity ($m.\ s^{-2}$)
Gr	Grashof number
H	Height of the two cylinders (m)
P	Pressure (Pa)
Pr	Prandtl number
(r,θ,z)	Cylindrical coordinates (m or rad)
Re	Reynolds number
Re_C	Critical Reynolds number
Re_r	Relative Reynolds number
r_i	Inner cylinder radius (m)
r_o	Outer cylinder radius (m)
t	Time (s)
T	Temperature (K)
T_0	Average temperature (K)
T^*	Dimensionless temperature
V_r	Radial velocity ($m.\ s^{-1}$)
V_θ	Azimuthal velocity ($m.\ s^{-1}$)
V_z	Axial velocity ($m.\ s^{-1}$)
V_r^*	Dimensionless radial velocity
V_θ^*	Dimensionless azimuthal velocity
V_z^*	Dimensionless radial velocity
$\boldsymbol{u}$	Vector Velocity ($m.\ s^{-1}$)
U_{ts}	Terminal velocity ($m.\ s^{-1}$)

Greek symbols

α	Thermal diffusivity ($m^2.\ s^{-1}$)
β	Thermal expansion (K^{-1})
Γ	Height-to-gap aspect ratio
η	radius-ratio
μ	Dynamic viscosity ($Pa.\ s$)
ν	Kinematic viscosity ($m^2.\ s^{-1}$)
ω	Rotational velocity ($rad.\ s^{-1}$)
ρ	Density ($kg.\ m^{-3}$)

Notation

CCF	Circular Couette Flow
TVF	Taylor vortex flow
WVF	Wavy vortex flow
$(.)_i$	Inner cylinder
$(.)_o$	Outer cylinder
$(.)_P$	Particles

[8] explain how the boundary conditions of end-walls may be used to describe the dynamics of RHISCO experiments. Using linear stability analysis and direct numerical simulations, they determined a criterion to determine if the laminar heat transfer is conductive or convective by nature. Also, they confirmed that flow instabilities are driven by the interaction of thermal buoyancy and cylinder rotation mechanisms.

In many practical applications such as in dynamic filtration processes, the fluid may drive particles with different sizes and shapes. The particle deposition along the walls generates sedimentation which will cause a decrease of the thermal and mechanical efficiencies. A comprehensive review of annular centrifugal contactors was developed by Vendantam and Joshi [12] for single and multiphase flow patterns and different drop and bubble size distributions. For rotating filters, Wereley and Lueptow [13] attested that for particles having a higher density than the base fluid, the particle paths deviate significantly from the fluid streamlines due to the interaction between the centrifugal force and the drag force. By a combined experimental and numerical approach, Nemri et al., [16] showed that the mixing axial dispersion of particles is enhanced when the Reynolds number increases. The mixing behavior depends also strongly on the flow regime, mainly for the wavy flow regimes (WVF and MWVF) where a multiplicity of stable wavy states can be reached.

Moreover, the Couette apparatus is used to classify particles and measure many important particle properties such as particle density, fractal dimension, aerosol mass distributions, and dynamic shape factors [15]. In fact, the centrifugal particle mass analyzer (CPMA) classifies particles by their mass-to-charge ratio and uses a stable system of forces to improve the transfer function of the classifier compared to the aerosol particle mass (APM) analyzer [16].

Therefore, for Taylor-Couette regime, inertial effects generate a significant amount of particle loss and it is inconvenient to use CMPA in the Taylor vortex regime [15]. To improve the design and achieve a more accurate classification, it is an important to understand the particle trajectories inside the Taylor-Couette apparatus.

For light non-spherical and heavy spherical particles, the experimental results of Qiao et al. [17] showed that the particle trajectories inside the Taylor-Couette device are strongly dependent on the particle density and Reynolds number.

For experimental set-up design, S. P. Bhattacharya [18] has warned that apparent emittance of a non-isothermal particulate deposit could be significantly different from the isothermal emittance if there is a substantial temperature gradient across it and the deposit is composed of transparent material or coarse particles.

Most recently, experimental investigation Majji et al. [19] has been performed to study the particles behaviors (Dp = 350 mm) inside Taylor-Couette device ($\eta = 0.877$, $\Gamma = 20.5$) for different flow regimes (CCF, TVF, WVF). Experimental visualization permitted to explain the mechanism of particles migrations for different Taylor-Couette flow regimes. However, the thermal effects on the flow structure and particle behavior were not considered so far.

The first part of this paper aims at studying the combined effects of rotation and natural convection on the dynamic and thermal structures for a Taylor-Couette flow arrangement with a low aspect ratio compared to the former works of [10,11]. Different Reynolds numbers are considered covering two flow regimes: circular Couette flow (CCF) and Taylor vortex flow (TVF). The different flow regimes produced by buoyancy-driven effects are identified through a power spectral density analysis of the azimuthal velocity. The second objective is to investigate the particle behaviors and their deposition time along the different walls for buoyancy-driven Taylor-Couette flows. For that, 10^5 particles of different diameters (35, 25, 15 and 10 μm) are injected at random positions inside the annular space once the steady-state flow is reached. The particles are followed by Lagrangian particle tracking method and particle time depositions are described for several Reynolds and Grashof numbers. To the best of the authors knowledge, it has never been considered so far in the literature.

2. Numerical methodology

2.1. Geometrical modeling

One considers the air flow between two coaxial cylinders (Fig. 1),

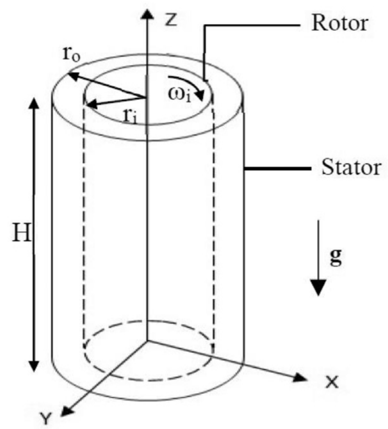

Fig. 1. Schematic of the Taylor-Couette flow arrangement.

disposed along the vertical z-axis. The radii of the inner and outer cylinders are fixed to $r_i = 45.72$ mm and $r_o = 62.85$ mm, respectively and their height is fixed to H = 400 mm. The gap size is then $d = r_o - r_i = 17.13$ mm. The Taylor-Couette cavity can be defined considering the radius-ratio $\eta = r_i/r_o = 0.727$ and the length-to-gap aspect ratio $\Gamma = H/(r_o - r_i) = 23.35$. This is to be compared to the recent simulations of Viazzo and Poncet [10] for $\eta = 0.8$ and $\Gamma = 80$.

The inner cylinder rotates counterclockwise at a fixed rotation rate denoted ω_i and is maintained at a temperature T_{ri}. The outer-cylinder is stationary and maintained at $T_{ro} < T_{ri}$. It is noteworthy that the sign of the radial temperature gradients has no significant influence on the stability of Taylor-Couette flows as reported experimentally by Guillerm [11] and confirmed numerically by Viazzo and Poncet [10]. The end-walls are considered adiabatic and stationary (Fig. 1). The different test cases are summarized in Table 1. The flow is controlled by the Reynolds and Grashof numbers (Table 1). The Reynolds number Re_i is defined as the ratio of centrifugal force to viscous force ($Re_i = \omega_i\, d\, r_i/\nu$), while the Grashof number Gr represents the ratio of buoyancy force to the viscous force ($Gr = g\beta\Delta T d^3/\nu^2$). The air properties ($Pr = 0.7$) are considered at the average temperature $T_0 = (T_i + T_o)/2$.

For a fixed outer cylinder, as the rotational speed of the inner cylinder increases, the laminar flow becomes unstable compared to axisymmetric perturbations inducing Taylor vortices in the flow field. The origin of this primary bifurcation is due to the centrifugal instability, which appears above a certain critical value of the Reynolds number Re_c. The critical Reynolds number depends on the radius ratio of the cylinders η and the angular velocity of the two cylinders [20,21]. The primary bifurcation appears under the form of Taylor vortices for a critical Reynolds number close to $Re_c \approx 82.9$ for a radius ratio $\eta = 0.727$ (DiPrima and Swinney, 1981). In this paper, one considers $0.81 \leq Re/Re_C \leq 4.47$, crossing circular Couette flow (CCF) to Taylor vortex flow (TVF) (Table 1), after DiPrima and Swinney [22] and Andereck et al. [23].

2.2. Governing equations

The Taylor-Couette cavity confined between two rotating cylinders with a weak radial thermal gradient is filled with an incompressible and Newtonian fluid. The fluid flow and heat transfer are governed by the conservation equations of mass, momentum and energy in their unsteady forms. The equations are written in cylindrical coordinates (r, θ, z):

Mass conservation equation:

$$\nabla.\,\mathbf{u} = 0 \tag{1}$$

Momentum conservation equations:

$$\rho_0\left(\frac{\partial\mathbf{u}}{\partial t} + \mathbf{u}.\,\nabla\mathbf{u}\right) = -\nabla P + \mu\nabla^2\mathbf{u} + \rho\mathbf{g} \tag{2}$$

Energy conservation equation:

$$\frac{\partial T}{\partial t} + \mathbf{u}.\,\nabla T = -\alpha\nabla^2 T \tag{3}$$

The flow is supposed to be 3D unsteady. The Boussinesq approximation is applied for the buoyancy term in the momentum equations (Eq. (2)), but otherwise the fluid properties are assumed to be constant. Under the Boussinesq approximation, the fluid density is equal to the reference density ρ_0 in all equations except for the buoyancy term in the momentum equation where the density is evaluated as:

$$\rho = \rho_0(1 - \beta(T - T_0)) \tag{4}$$

where T_0 is the average temperature which is the arithmetic mean between the hot and cold wall temperatures. Note that the Boussinesq approximation remains valid for small temperature differences, typically $\Delta T < 20$ for air [24] as it is the case here (see Table 1). Temperature levels are also sufficiently low to prevent from any evaporation effects.

2.3. Numerical modeling

The 3D conservative equations are solved in their unsteady form using the software ANSYS Fluent 14.5 based on the finite volume method [25]. The SIMPLE algorithm [26] is applied to overcome the pressure–velocity coupling. A QUICK scheme is used for the spatial discretization of all terms together with a second order implicit scheme for the temporal integration. The gradients are computed according to the Green-Gauss Cell-Based method.

Collocated meshes for the velocity components are used to prevent the development of numerical instabilities throughout the pressure field. A three-dimensional structural non-uniform grid arrangement has been considered (Fig. 2) and different grid sizes have already been tested previously [27]. The selected mesh is composed of (20 × 100 × 300 nodes) along the (r, θ, z) directions respectively and guarantees to provide mesh independent solutions for all Reynolds and Grashof numbers considered here. As shown in Fig. 2, the grid is refined close to the walls. In all cases, the time step is chosen so that the Courant number is always lower than 1.

Note that one first imposes a radial temperature gradient between the two cylinders without rotation. After the steady state solution is attained, the inner cylinder is gradually rotated with different angular velocities.

2.4. Validation of the flow solver

For laminar Taylor-Couette flows without radial temperature gradient between the two cylinders, the base flow is a laminar circular Couette flow far from the upper and lower disks and the velocity vector reduces to $\boldsymbol{u}(0, V_\theta(r), 0)$ for $\Gamma \to \infty$. For a weak radial temperature gradient between two stationary cylinders, a radial stratification of the density induces a baroclinic flow characterized by a large convection cell within the gap. Far from the disks, an axial upward flow is induced along the inner hot wall and by conservation of mass, fluid moves

Table 1
Values of the operating parameters.

radius-ratio $\eta = r_i/r_o$	0.727			
aspect ratio $\Gamma = H/(r_o - r_i)$	23.25			
Rotation rate ω of the inner cylinder (rad/s)	1.256	2.093	5.233	7.327
Inner Reynolds number Re_i	67.3	112.2	280.5	392.7

Temperature gradient $\Delta T = T_{r_i} - T_{r_o}$ (K)	1	2	5
Grashof number Gr	764.4	1528.9	3822.1

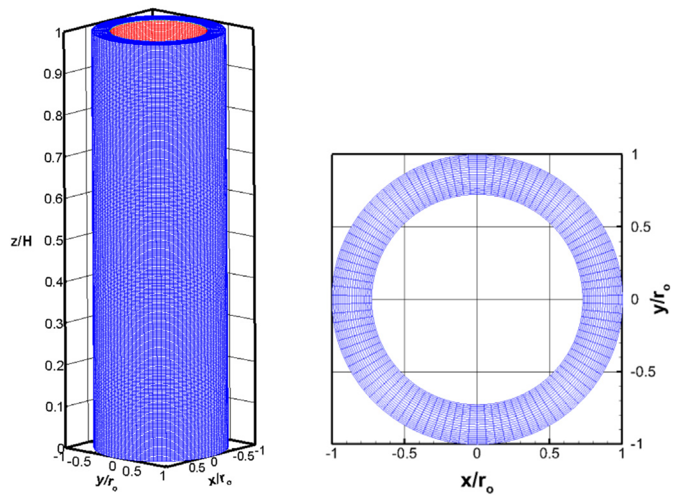

Fig. 2. 3D view and 2D view in a (r,Θ) plane of the structured mesh grid.

downwards close to the outer cold wall. The axial velocity component $V_z(r)$ depends only on the radial position r. The radial velocity $V_r(r)$ becomes significant in the vicinity of the endcap stationary disks. When both effects coexist ($\Omega \neq 0$, $\Delta T \neq 0$),the two base flows are superimposed and consequently there is an rivalry between the centrifugal force in the radial direction and the gravity force/buoyancy in the axial direction.

For low rotation rates of the inner cylinder and a weak temperature gradient, the analytical solutions for the dimensionless axial V_z^* and azimuthal velocity V_θ^* components and temperature $T^*$are written as follows (see in [10] for example):

$$V_z^*(r) = \frac{V_z(r)}{\beta \Delta T g \frac{d^2}{\nu}} = AB\left[(1-\eta)^2\left(\frac{r}{d}\right)^2 + (1-\eta^2)T^*(r) - 1\right] - 4A \left[(1-\eta)^2\left(\frac{r}{d}\right)^2 - \eta^2\right]T^*(r)$$

where

$$A = \frac{1}{16(1-\eta)^2},\ B = \frac{(1-\eta^2)(1-3\eta^2) - 4\eta^4\ln(\eta)}{(1-\eta^2)^2 + (1-\eta^4)\ln(\eta)} \tag{5a}$$

$$V_\theta^*(r) = \frac{V_\theta(r)}{\omega_i r_i} = \frac{\eta}{1+\eta}\left[-\frac{r}{d} + \frac{1}{(1-\eta)^2}\frac{d}{r}\right] \tag{5b}$$

$$T^*(r) = \frac{T(r) - T_i}{\Delta T} = \frac{\ln[(1-\eta)r/d]}{\ln(\eta)} \tag{6}$$

To validate the flow solver for the laminar circular Couette flow (CCF) with a radial temperature gradient, the azimuthal $V_\theta(r)$ and axial $V_z(r)$ velocity components and temperature profiles $T(r)$ obtained by the model are compared to the analytical solutions (Eqs. (5a), (5b) and (6)) in Fig. 3. For $Re_i = 56$ and $Gr = 1425.3$, the present results are in perfect agreement with the analytical solutions for CCF with a radial temperature gradient. The temperature and azimuthal velocity profiles exhibit a weak curvature due to the high value of the radius ratio $\eta = 0.727$. A weak asymmetry is observed for the axial velocity component induced by the curvature of the system and inflexion points may be observed. This profile may become unstable to infinitesimal perturbations after the Rayleigh criterion, leading to different modes of instability.

3. Buoyancy-driven instabilities

3.1. Flow structure without buoyancy effects

The flow configuration without buoyancy effects, which means that the fluid density is constant, the computed contours of temperature and velocity vectors are represented in Fig. 4 for different Reynolds numbers and a given Grashof number $Gr = 1528.9$. The dynamic and

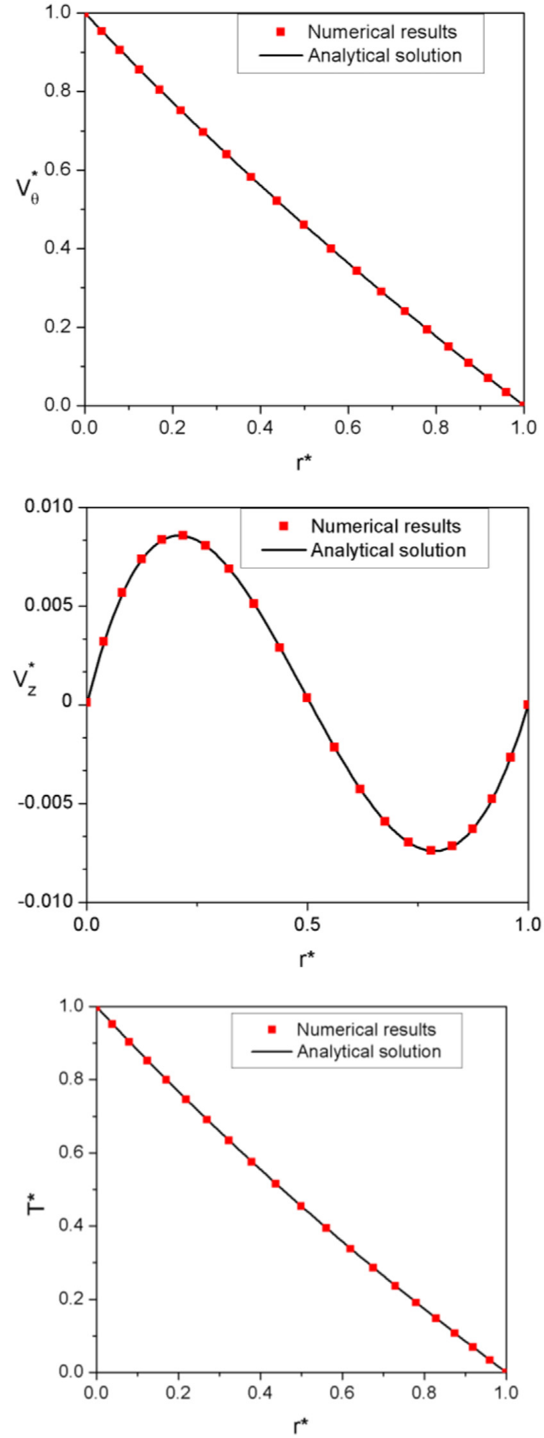

Fig. 3. Validation of the present numerical solver against the analytical solution for radial distributions of the dimensionless azimuthal V_θ^* and axial V_z^* velocity components and the temperature T^* for $Re_i = 56$ and $Gr = 1425.3$ at mid-height.

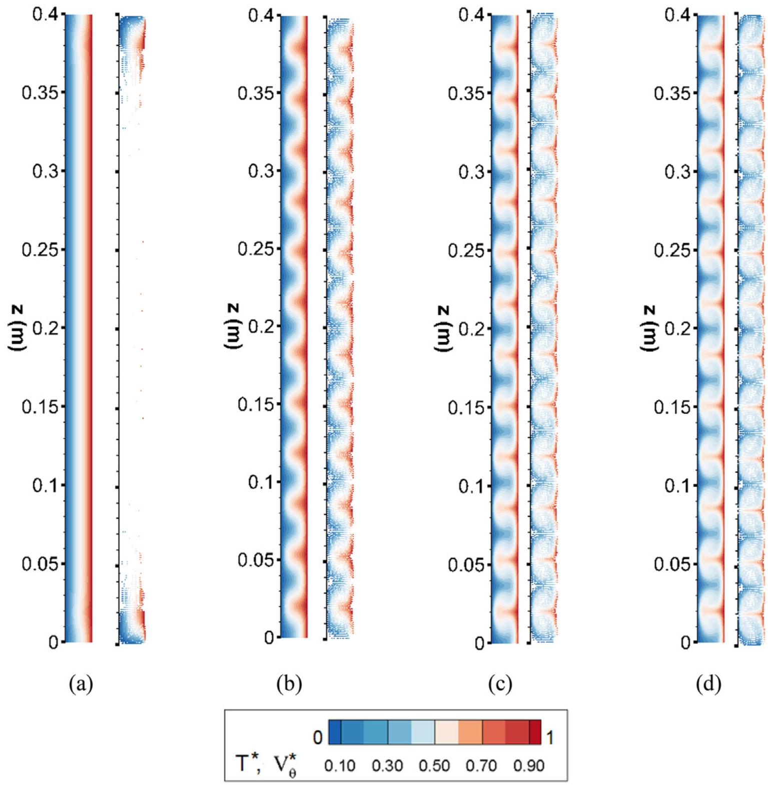

Fig. 4. Temperature and velocity vectors contours for different Reynolds numbers: (a) $Re_i = 67.3$, (b) $Re_i = 112.2$, (c) $Re_i = 280.5$ and (d) $Re_i = 392.7$. Results obtained for constant density and $Gr = 1528.9$. Blue color: T_{min} and V_{min} on the stator; Red color: T_{max} and V_{max} on the rotor. (For interpretation of the references to color in this figure legend, the reader is referred to the web version of this article.)

thermal structures show clearly that the flow covers different flow regimes: circular Couette flow ($Re_i = 67.3$) and vortex Taylor flow ($Re_i = 112.2$, 280.5 and 392.7). For circular Couette flows, the flow is characterized only by vortices close to the end walls of toroidal shape named Eckman vortices (Fig. 4a). These first vortices are generated by the presence of the end walls and are not detected for infinite cylinders ($\Gamma \to \infty$). In the middle of the annular space, the flow remains parallel to the cylinders without vortical structures. Similarly, isotherms contours are parallel revealing that the flow occurs without thermal stratification and heat transfer is purely a conductive process.

When the angular velocity of the inner cylinder is increased above a certain critical value ($Re/\mathrm{Re_C} > 1$), the circular Couette flow becomes unstable to the centrifugal instability leading to the onset of a secondary steady state. It is characterized by axisymmetric and time-independent toroidal vortices, identified as Taylor vortex flow (Fig. 4b–d). As shown on Fig. 4, the flow is described by a regular cellular vortex structure in which 24 ($\sim \Gamma$) counter-clockwise ring vortices are observed. Two adjacent vortices are separated by regular thermal plumes going from the rotor to the stator. Coughlin and Marcus [28] indicated that such flow is dominated by an outflow jet, which is driven directly by the centrifugal force, and which tends to eject the fluid from the rotating inner cylinder. By increasing Reynolds number, the radial force becomes more dominant and drives the plumes towards the outer-cylinder (Fig. 4c,d).

In the present cases, the average length of the rings is about $l = 3.34$ *cm* generating 12 pairs of vortices along the vertical direction. For finite-size cylinders, the rings close to the end-walls are more important than that in the center of the cavity due to the end-wall effects. The same results were observed experimentally by Koschmieder [29] for cylinders of height $H = 84.9$ *cm* and $\Gamma = 49.56$. He found an average length of $l_1 = 3.46$ *cm* for a comparable radius ratio $\eta_1 = 0.727$.

3.2. Buoyancy effects on the Taylor-Couette flow structures

One considers now that the density is a function of the fluid temperature. The gravitational force is then added to the balance forces in the momentum equations. For the flow confined between differentially heated cylinders, the temperature gradient produces a radial stratification of density. The coupling between the buoyancy and Archimedes forces induces a upward flow close to the hot wall and downward flow near the cold wall, engendering then a large convection cell within the annular space. By increasing the Reynolds or Grashof numbers, the flow can get more complex. Contours of temperature and velocity vectors are represented in Fig. 5 for different Reynolds and Grashof numbers. For low Reynolds numbers $Re_i = 67.3$, the buoyancy effect is explicitly visible and the circular Couette flow is destabilized by natural convection. The additional vertical velocity initiated by the radial temperature gradient along the heated cylinders drives the Ekman vortex close to the top disk. The isotherms confirm the dominating character of the free convective heat transfer.

At a given Grashof number, if one increases the inner Reynolds number, the effects of buoyancy decrease relatively but somewhat remain observable. For $Gr = 3822.1$ as an example, the convection cell obtained at $Re_i = 67.3$ gets destabilized at $Re_i = 112.2$ with the appearance of irregular Taylor vortices. At $Re_i = 280.5$, they get more organized with a given axial wave number. Increasing further the Reynolds number up to $Re_i = 392.7$, the axial wave number slightly decreases. In the same way, at a given Reynolds number $Re_i = 112.2$, Fig. 5 confirms that the Taylor vortices are driven by buoyant force close to the heated cylinders, consequently they cause a totally unstable and time-dependent vortex flow. The flow becomes increasingly complex by increasing the radial thermal gradient between the two cylinders with a more intense and larger vortex at the corner between the inner cylinder and the upper end-cap disk.

Fig. 6 displays the isosurfaces of the radial velocity used to highlight the coherent vortices appearing within the flow. It is noteworthy that the accounting for the buoyancy effects significantly affects the patterns, changing from regular Taylor vortices to the onset of regular spirals (SPI) (Fig. 6b), which appear only on the upper half of the cavity. This axial asymmetry has already been reported experimentally by Andereck et al. [23] then Lepiller et al. [4] and Guillerm [11] for $\eta = 0.8$ and $\Gamma = 114$. Increasing further the Grashof number leads to

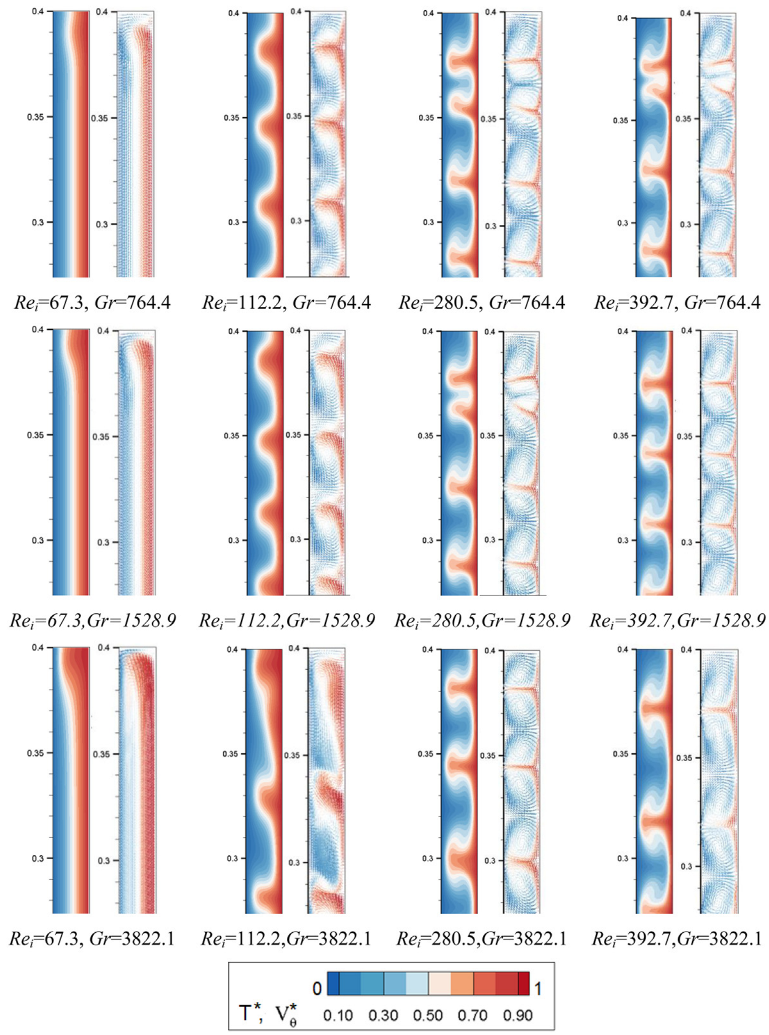

Fig. 5. Temperature contours and velocity vectors for different Reynolds and Grashof numbers. Results obtained for variable density $\rho = f(T)$. For sake of clarity, only the top part of the cavity is shown here.

the wavy spiral (WSPI) regime confirming the former DNS results of Viazzo and Poncet [10] for $\Gamma = 80$ (Fig. 6c). However note that the critical Reynolds and Grashof numbers for the transition between the SPI and WSPI regimes are different to that obtained by Viazzo and Poncet [10] due to the different aspect ratios. The regimes shown in Fig. 6 are obtained for a Taylor number $Ta = Re_i\,(d/r_i)^{1/2} = 68.7$ and Rayleigh numbers $Ra = Gr \times Pr$ ranging between 535.1 and 2675.5. For this range of parameters, Viazzo and Poncet, [10] reported only a wavy vortex flow in agreement with the experimental results of [11]. Finally, for $Gr = 3822.1$ (Fig. 6d), one gets a complex flow regime, which combines irregular wavy spirals and a Taylor vortex flow. It can be seen as the onset of the SPI + WVF regime.

For the highest Reynolds numbers considered here, the centrifugal force reduces the buoyancy effects but the vortices remain still time-dependent. In order to fully characterize these flow regimes, a spectral analysis of the time series is required.

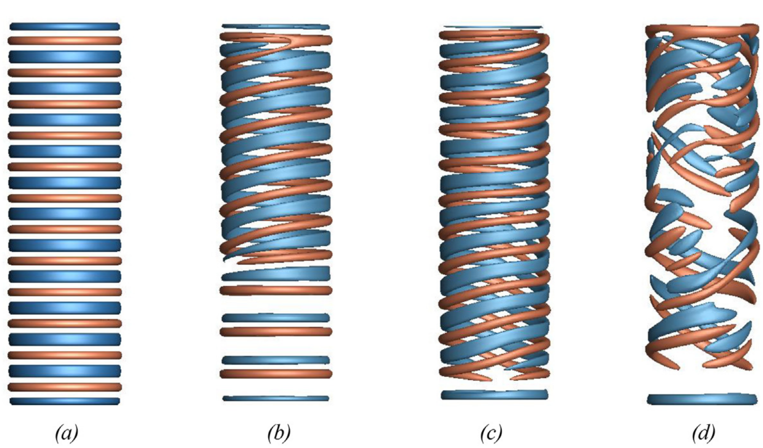

Fig. 6. Isosurfaces of the radial velocity for $Re_i = 112.2$ and: (a) $Gr = 764.4$ (constant density), (b) $Gr = 764.4$ (variable density), (c) $Gr = 1528.9$ (constant density) and (d) $Gr = 3822.1$ (constant density). Blue: isovalue $V_r = -0.004$ m/s, red: isovalue $V_r = 0.005$ m/s. (For interpretation of the references to color in this figure legend, the reader is referred to the web version of this article.)

3.3. Spectral analysis of the tangential velocity temporal series

A power spectral density (PSD) is performed here to analyze the Taylor-Couette regimes previously shown in Fig. 6. For $Re_i = 112.2$, the temporal series of the azimuthal velocity are plotted for different Grashof numbers with their Fourier transform (Fig. 7).

For Gr = 764.4, the flow is characterized by the coexistence of spiral patterns and Taylor vortices (Fig. 6b). The power spectrum deduced from the temporal series of the azimuthal velocity indicates that the flow occurs with a fundamental frequency ($f/f_i = 0.342$) and three harmonics (2f, 3f, 4f) (Fig. 7b). According to the experimental results of Andereck et al. [23], the signal corresponds to the spiral vortices.

For Gr = 1528.9, the flow becomes unstable with a spiral vortex regime along the cylinders (Fig. 6c). However, the signal begins to be disturbed and the frequency spectrum indicates that the frequencies are independent (without any harmonic). The flow reaches a transition regime. As seen in Fig. 7b, the three frequencies in the power spectrum indicate that the spiral flow is modulated by a low frequency ($f/f_i = 0.324$).

For Gr = 3822.1, the vortices are completely destroyed by natural convection producing a more chaotic flow (Fig. 6d). This flow becomes progressively complex when temperature gradient is increased. The signal and Fourier transform of the azimuthal velocity signal confirm the chaotic character of the flow by the presence of disordered structures around the modulation frequency ($f/f_i = 1.048$) (Fig. 7c). Nemri et al. [14] designated this turbulent flow as a weakly turbulent regime, knowing that for a fully turbulent flow, the power spectrum would have no dominant frequency.

However, as the Reynolds number increases from $Re_i = 280.5$ to $Re_i = 392.7$, the Taylor-Couette flow reaches a spiral flow regime ($f/f_i = 0.217$) without attaining the turbulent flow for the temperature gradients considered in this paper (Fig. 8).

4. Particle deposition

4.1. Lagrangian particle tracking

In this section, one investigates the particle trajectories of water droplets driven by the buoyancy driven Taylor-Couette flow inside a differentially heated cavity. The particle trajectories are calculated by a Lagrangian approach, where the particles are treated as a discrete phase made of spherical particles dispersed in a continuous phase. The particle volume loading is usually assumed to be negligible, so that the particles have no feedback effect on the air flow and particle-particle interactions are neglected. Recent experimental results by Majji et al. [19] indicate that different Taylor-Couette flow regimes (CCF, TVF, WVF) are not significantly affected by particle diameters of $D_p = 350$ μm. Also, the one-way coupling is considered for fluid-particle interactions, which means that the fluid drives the particle phase via drag and gravitational forces. For the particle diameters considered in this work, Brownian diffusion [30] and lift force [31] are neglected.

The trajectory is calculated by integrating the following equation for the particles:

$$\frac{du_P}{dt} = F_D(u - u_P) + g(\rho_P - \rho)/\rho_p \tag{7}$$

where u is the fluid velocity, u_p is the particle velocity, ρ_p the particle density and F_D is the drag force, which can be expressed per unit mass as:

$$F_D = \frac{18\mu}{\rho_P D_P^2} C_D \frac{\mathrm{Re}_r}{24} \tag{8}$$

with D_p the particle diameter, μ the fluid dynamic viscosity and Re_r the relative Reynolds number defined as:

$$\mathrm{Re}_r = \frac{\rho_P D_P\ |u - u_P|}{\mu} \tag{9}$$

The drag coefficient C_D is given by:

$$C_D = a_1 + \frac{a_2}{\mathrm{Re}_r} + \frac{a_3}{\mathrm{Re}_r^2} \tag{10}$$

where a_1, a_2 and a_3 are constants that apply to smooth spherical particles over several ranges of Reynolds numbers [25,32]. The virtual mass and pressure gradient forces are not significant since the density of water droplets exceeds considerably the air density: $\rho_p \gg \rho$. Also, the recent work of Dehbi et al. [33] indicates that the thermophoretic force has only a very weak influence on the deposition rates and deposition patterns for particles larger than 1 μm. Finally, the lift force may be also neglected, as a first approximation, as it is magnitude is generally one or two orders of magnitude lower than the drag force for shear flows over a wide range of particulate Reynolds number as shown by Lataste et al. [34]. The lift force may become significant for turbulent shear

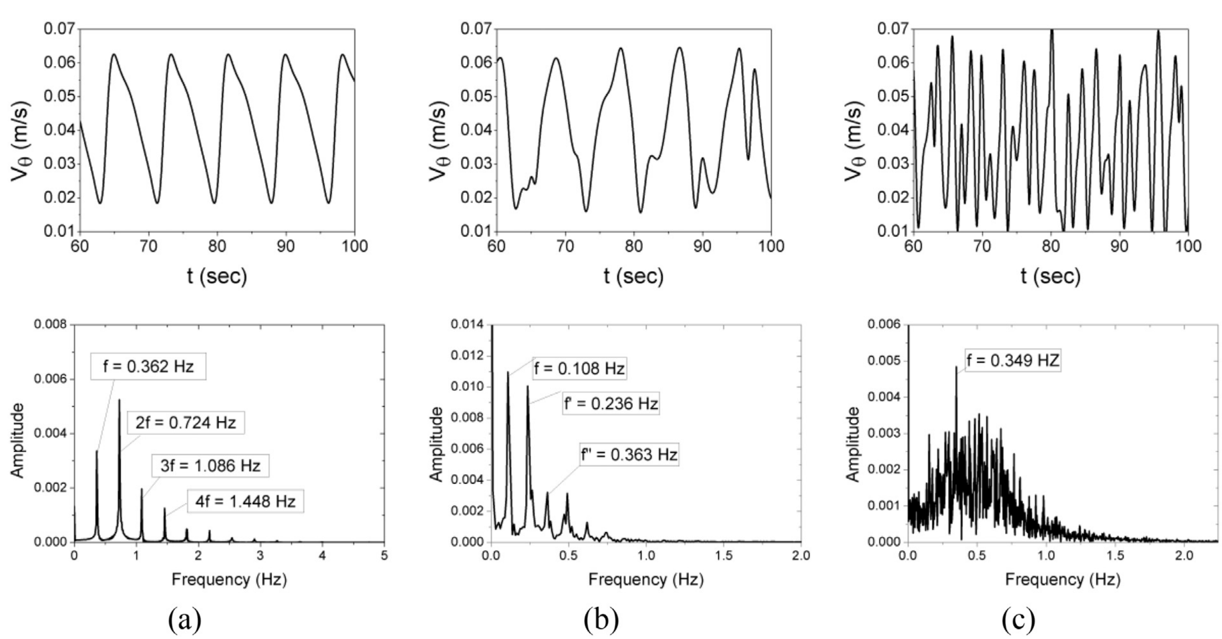

Fig. 7. Time series and power spectrum of the azimuthal velocity for $Re_i = 112.2$, variable density and: (a) $Gr = 764.4$, (b) $Gr = 1528.9$, (c) $Gr = 3822.1$.

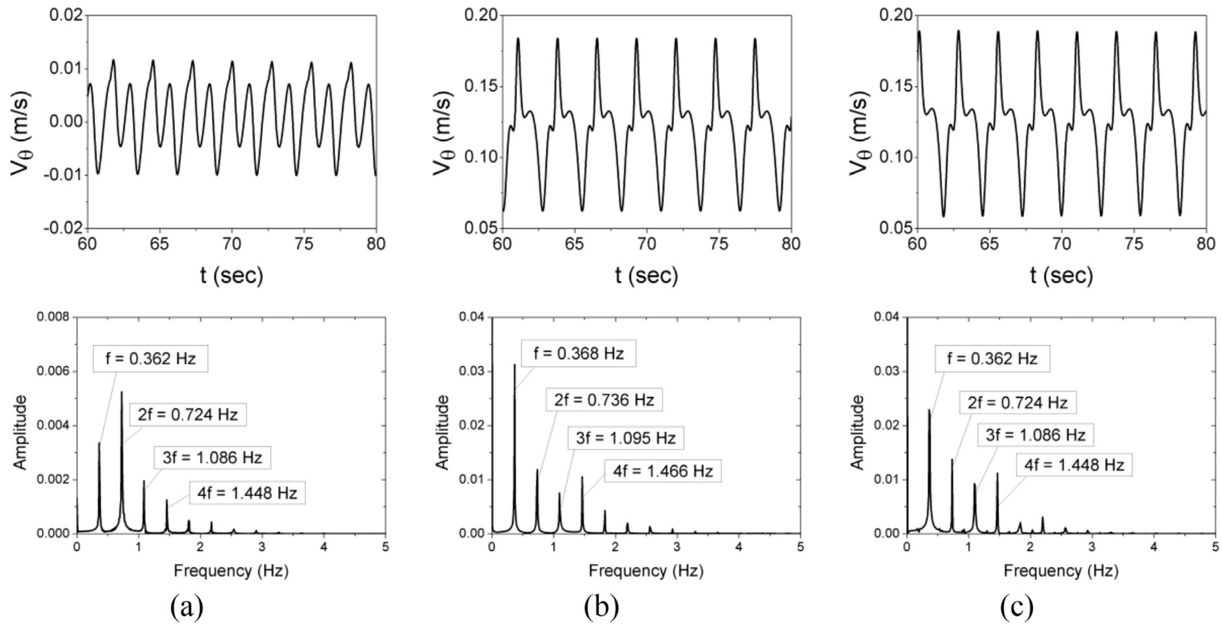

Fig. 8. Time series and power spectrum of the azimuthal velocity for $Re_i = 392.7$, variable density and: (a) $Gr = 764.4$, (b) $Gr = 1528.9$, (c) $Gr = 3822.1$.

Table 2
Terminal velocity for different particle diameters.

D_p (µm)	Terminal settling velocity UTS (m/s)	Time deposition t (s) for quiescent atmosphere and H = 0.4 m
35	3.55×10^{-2}	11.27
25	1.81×10^{-2}	22.06
15	6.56×10^{-3}	70
10	2.93×10^{-3}	136.48

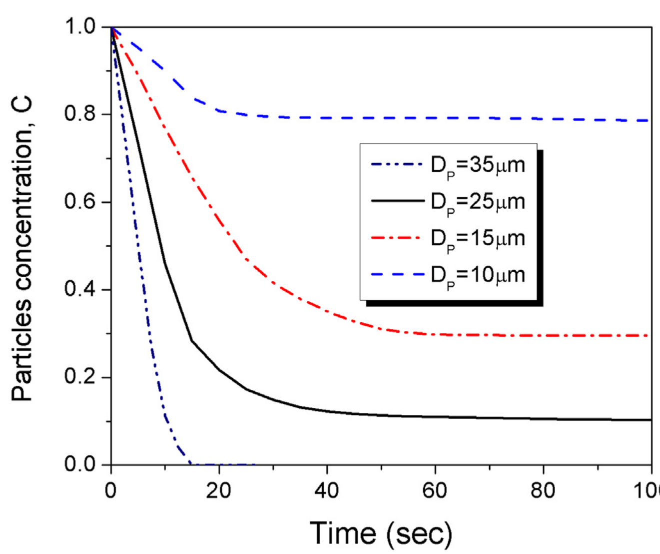

Fig. 9. Temporal evolutions of the suspended particle concentration for $Re_i = 112.2$, $Gr = 1528.9$ and different particle diameters (ρ = constant).

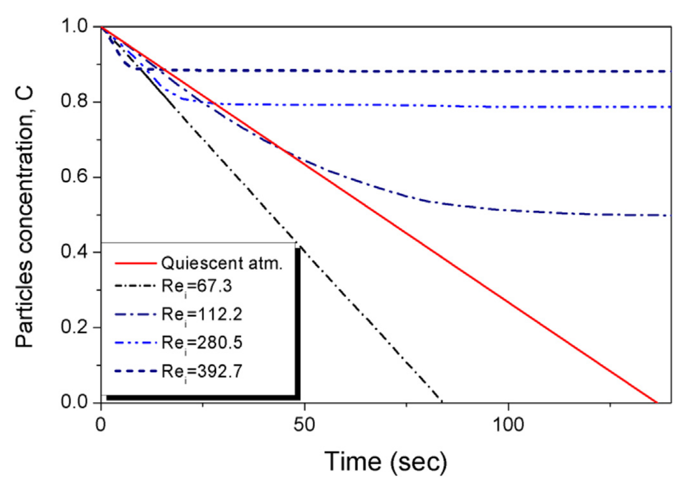

Fig. 10. Temporal evolutions of the suspended particle concentration for different Reynolds numbers. Dp = 10 µm and $Gr = 1528.9$ (ρ = constant).

flows but it is out of the scope of the present work.

For Lagrangian particle tracking, four different diameters ($D_p = 10$, 15, 25 and 35 µm) were considered and the water droplets injected at random positions inside the annular space for different Reynolds and Grashof numbers. Each injection is composed of $N_p = 10^5$ point-wise solid spheres having a diameter d_p and thermophysical properties of water ($\rho_P = 1000\ kg/m^3$, $\lambda_P = 4182\ W/(m.\ K)$). The injection velocity of the particles is set to zero and particle boundary conditions at the walls are considered as trap conditions.

At equilibrium, the Stokes drag force balances gravity force, so [35]:

$$F_D = m_p g = 3\pi\mu U_{TS} d_p \tag{11}$$

where U_{TS} is the terminal velocity given by:

$$U_{TS} = \tau_P\, g = C_c \frac{\rho_P d_P^2}{18\mu}\, g \tag{12}$$

where τ_p is the relaxation time, which depends on the particle and fluid properties. This parameter is important for the integration time because it characterizes the response time to particle acceleration. C_c is the Cunningham correction factor for submicron particles, for particle diameters considered in this paper, $C_c = 1$ [36]. Table 2 gives the terminal velocity according to the particle diameter and the corresponding time deposition along the height of H = 0.4 m for a quiescent atmosphere.

One defines also the particle concentration, which represents the ratio of the total number of injected particles N_p by the suspended particles inside the annular space at a given time t $N_{P,\ (time)}$ as follows:

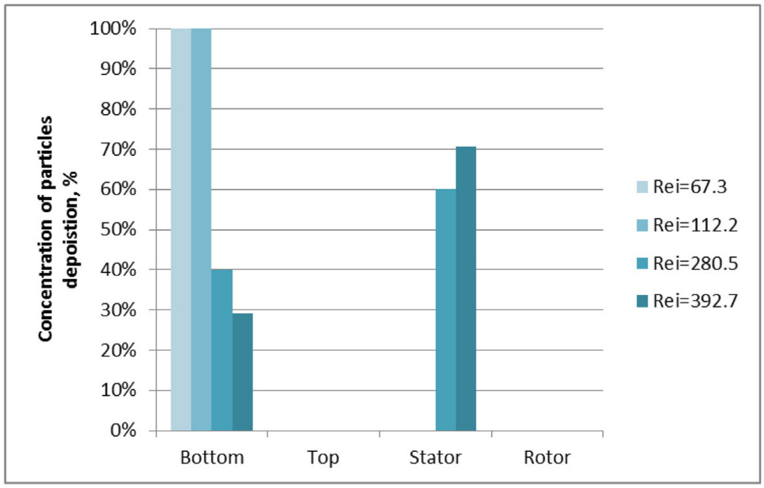

(a)

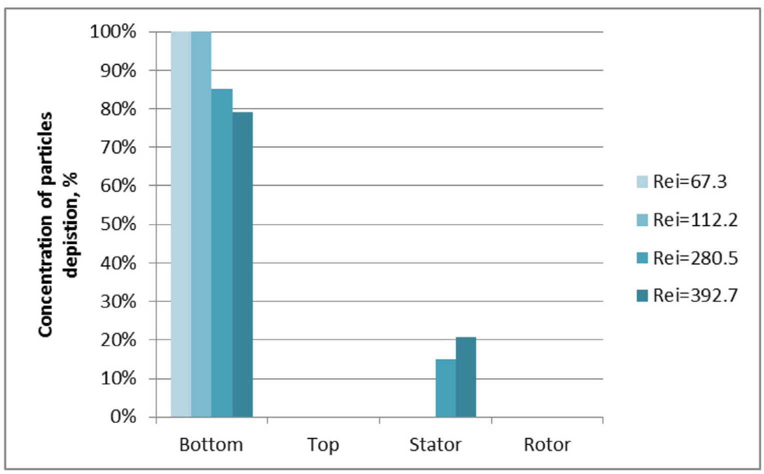

(b)

Fig. 11. Histograms of the particle deposition concentration along the bottom wall and stator for four Reynolds numbers Re_i: (a) D_p = 10 μm and (b) D_p = 15 μm. Results obtained for Gr = 1528.9 after t = 300 s. Note that the concentration is equal to 0 along the top wall.

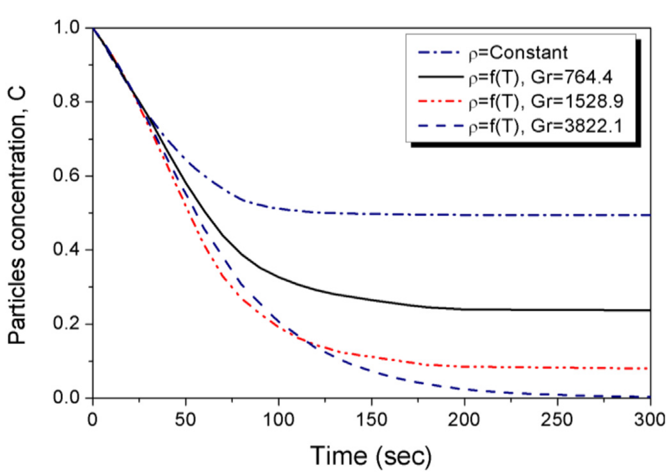

Fig. 12. Temporal evolutions of the suspended particle concentration for different Grashof numbers Gr with and without natural convection effects for Dp = 10 μm and Re_i = 112.2.

$$C_{(time)} = \frac{N_{p,(time)}}{N_p} \tag{13}$$

4.2. Influence of the particle diameter

In the case of a rotating flow without natural convection effects, the main physical parameters that characterize the particle trajectory inside the annular space are the rotation speed of the inner cylinder and the particle diameter. For the present configuration, the time evolution of suspended particle concentration is represented in Fig. 9 for different particle diameters and for a Reynolds number Re_i = 112.2. The particles of larger diameter (D_p = 35 μm) drop rapidly by gravity. Almost all the particles disappear completely between the two cylinders at t = 14.85 s. For smaller particles, the concentration decreases until reaching an asymptotic value: $C_{(25\mu m)}$ = 0.1, $C_{(15\mu m)}$ = 0.3 and $C_{(10\mu m)}$ = 0.3. Likewise, Fig. 9 indicates that the drag force becomes gradually predominant over the gravity force for smaller particles, thereby generating a better particle suspension. For heavier particles (D_p = 350 μm) not considered here, experimental visualizations by Majji et al. [19] showed that the particles have sufficient time to reach their equilibrium locations inside CCF and TVF flow regimes which are invariant in the azimuthal direction. In contrast, the WVF is characterized by azimuthal waviness in each vortex which induces the axial oscillations. The particles remain thus mixed in the annular region without attaining an equilibrium location [19].

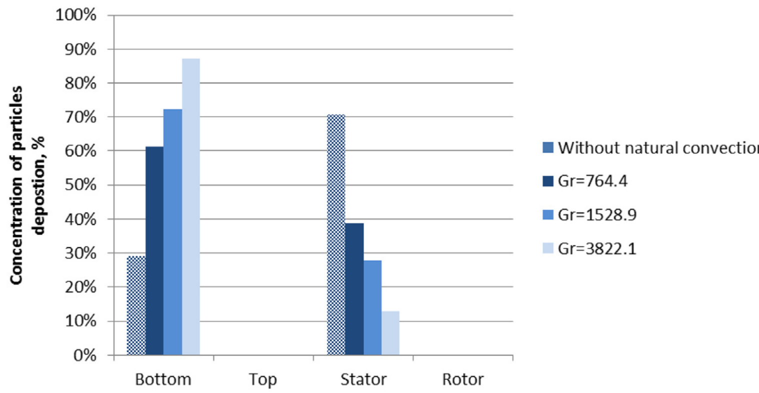

Fig. 13. Histograms of the particle deposition concentration along the bottom wall and stator for different Grashof numbers *Gr*. Results obtained for Dp = 10 μm, Re_i = 392.7 after t = 300 s.

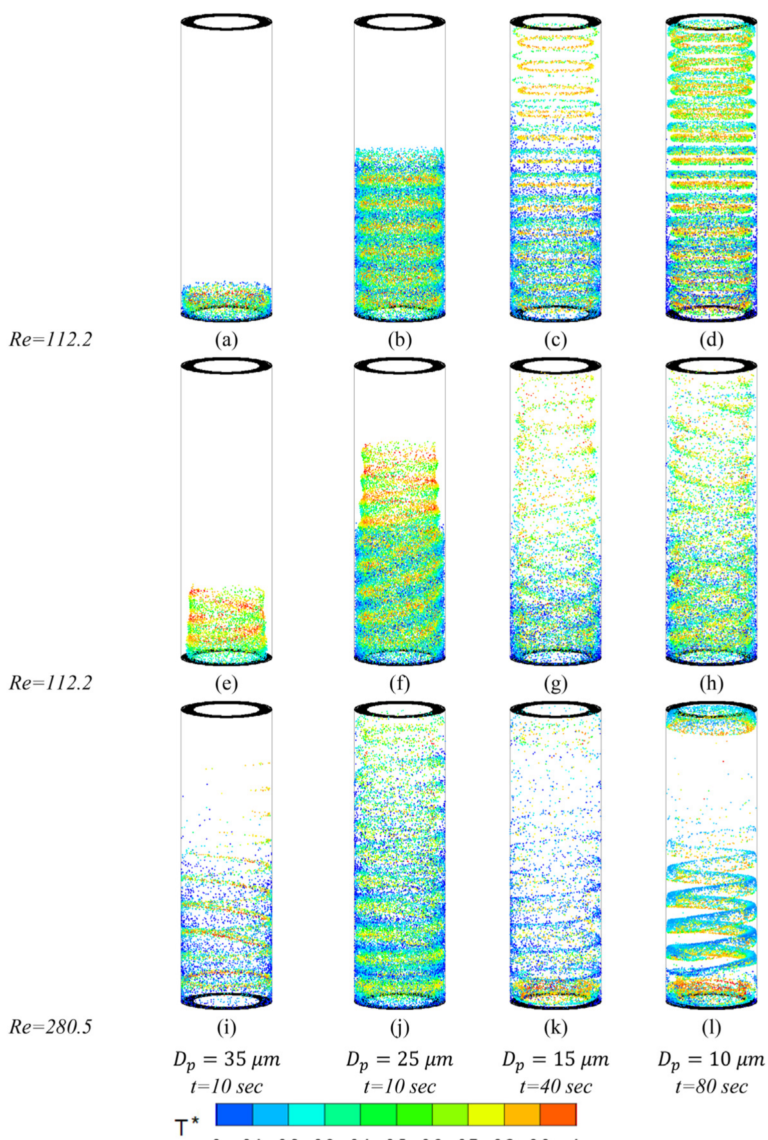

Fig. 14. Snapshots of particle locations at different times and for different particle diameters: (a–d) density is constant and (e–l): ρ = *f*(*T*). Results obtained for *Gr* = 1528.9. The particles are colored by their temperature.

4.3. Influence of the inner Reynolds number

The influence of the Reynolds number on the particle deposition is displayed in Fig. 10 for a particle diameter $D_p = 10$ µm and different Reynolds numbers: $Re_i = 67.3$ (CCF) and $Re_i = 112.2$, 280.5 and 392.7 (TVF). For Couette flow, the particles fall down linearly versus time and disappear at $t = 84$ s. However, the presences of Ekman vortices close to the end-walls influence similarly the particle deposition. In fact, in a quiescent atmosphere with height H = 0.4 m, the deposition time of all particles ($D_p = 10$ m) inside the cavity is achieved at $t = 136$ s. At $Re_i = 67.3$, the particle deposition is even faster, which represents a peculiar behavior compared to what is obtained for the other Reynolds numbers. In fact, the Ekman vortices located to the end-cap disks generate a local acceleration responsible for this short deposition time. At higher Reynolds numbers, the rotation of the inner cylinder creates the main tangential flow and the presence of Taylor vortices accentuate the residence time of the particles, which remain in suspension as being trapped by the vortices. So by increasing the Reynolds number, the deposition time increases. The suspended particle concentration tends towards an asymptotic value: $C_{(Rei=112.2)} = 0.49$, $C_{(Rei=280.5)} = 0.79$ and $C_{(Rei=392.7)} = 0.88$ for $D_p = 10$ µm.

Similarly, the rotation velocity of the inner cylinder has another very important effect on the driven particles, acting mainly on the particle deposition on the walls. The concept concerns the sedimentation process on different walls, which is an interesting industrial application subject for dynamic filtration process among other example. Fig. 11 shows the concentration of deposited particles on the different walls inside the Taylor-Couette apparatus at $t = 300$ s. For a flow close to the critical Reynolds number ($Re_i = 67.3$ and 112.2), the dropped particles are totally accumulated on the bottom wall for both values of the particle diameter, $D_p = 10$ µm and 15 µm (Fig. 11a,b). However, by increasing the Reynolds number up to $Re_i = 280.5$ and 392.7, other particles are driven by the centrifugal force to deposit on the stator. The wall deposition rate becomes more important along the stator by increasing Re_i. One can also note by comparing Fig. 11a,b that the centrifugal force is predominant on smaller (so lighter) particles resulting a greater accumulation of particles on the stator than on the bottom wall (29% for the bottom wall and 71% for the stator). For the Reynolds numbers considered in this work, there are no particles deposition on the rotor and the top wall.

4.4. Influence of the Grashof number

The influence of natural convection on the particle deposition is now investigated for a particle diameter equal to $D_p = 10$ mm by considering that the fluid density is a function of temperature. The corresponding suspended particle concentrations are presented in Fig. 12 for different Grashof numbers and $Re_i = 112.2$. The time evolutions profiles are compared to the case where the density is constant. Fig. 12 indicates that natural convection plays a very significant role in the deposition process of suspended particles inside the annular space. Moving from a Taylor Vortex flow to a spiral flow, natural convection not only accelerates the particle deposition between the cylinders, but generates a quasi-total deposition by increasing the radial temperature gradient. All the concentration profiles reach asymptotic values such that, after $t = 300$ s, $C_{(\rho=cste)} = 0.49$, $C_{(Gr=764.4)} = 0.24$, $C_{(Gr=1528.9)} = 0.08$, $C_{(Gr=3822.1)} = 0$.

Natural convection has the same effect on the particle sedimentation along the stator and bottom walls. In Fig. 13, the histograms of the accumulated particles along the walls obviously show that the particles tend to deposit completely on the bottom wall when the radial temperature gradient increases.

It appears that the coupled Taylor-Couette/buoyancy-driven flow drags more particles at bottom of apparatus. The gravitational force effect becomes significant for higher temperature gradients.

For constant density and buoyancy-driven flow, the instantaneous snapshots of particle locations at different times and for four particle diameters are illustrated in Fig. 14. It can be seen that particle deposition is more completed and accelerated for coarse particles. However, for fluid flow with constant density, the smaller particles ($D_P = 15$ and 10 µm) are confined inside Taylor vortices as shown in Fig. 14. Nevertheless, the formation of instabilities, due to the coupling between an azimuthal flow induced by rotation and an axial flow due to convection caused by the radial temperature gradient, will drive the particles into spiral vortices. Also, the trajectories of the particles highlight the inclined vortices compared to the cylinder axis and the buoyancy-driven flow induces significant effects on the sedimentation and the displacement of particles inside the Taylor-Couette apparatus.

5. Conclusion

In this paper, one considered the air flow between two cylinders differentially heated with rotating inner cylinder. The fluid density depends on temperature according to the Boussinesq approximation. The density variation close to the heated cylinders generates a strong coupling between the base Taylor-Couette flow and the natural convection inside the annular space. The flow regimes considered are Couette and Taylor Vortex flow regimes (CCF - TVF) for different Reynolds ($67.3 \leq Re_i \leq 392.7$) and Grashof ($764.4 \leq Gr \leq 3822.13$) numbers. The main results can be summarized as follows:

- The radial temperature gradient between the stator and the rotor destabilizes the Taylor vortex flow structures (TVF) and the Taylor vortices get driven by buoyancy force along the heated cylinders.
- An unsteady flow is highlighted until a complex flow regime is achieved for important radial temperature gradients and low Reynolds numbers.
- The natural convective flow decreases in intensity at high rotation rates; however, the flow remains unsteady and characterized by spiral vortices.

In order to study the particle behaviors inside the differentially heated Taylor-Couette cavity, water droplets of various diameters have been injected at different locations. The particle tracking indicates that:

- For high rotation velocities of the rotor, the centrifugal force drives more particles to sediment along the stator than on the bottom wall.
- The drag force becomes more significant when the natural convection is predominant, which tends to maintain more suspended particles inside the annular space.
- At a given Reynolds number, the deposited particles are driven to sediment more along the bottom walls when a radial temperature gradient is imposed compared to the case without radial temperature gradient or with constant density.

The conclusions drawn here could be extended to any solid particles having similar diameter and density.

Future work includes the extension of the present solid-liquid suspension model to account for a two-way coupling. Even if the particle distribution is diluted at early stages, particles tend to concentrate in specific flow regions and may become more densely distributed locally at specific times. A full two-phase solver would be then necessary to better simulate the particle deposition.

References

[1] A. Lalaoua, F. Naït Bouda, Numerical investigation of the onset of axisymmetric and wavy Taylor-Couette flows between combinations of cylinders and spherocylinders, Eur. Phys. J. Plus 133 (2018) 383.
[2] H.A. Snyder, S.K.F. Karlsson, Experiments on the stability of Couette motion with a radial thermal gradient, Phys. Fluids 7 (1964) 1696–1707.
[3] M.M. Sorour, J.E.R. Coney, The effect of temperature gradient on the stability of flow between vertical, concentric, rotating cylinders, J. Mech. Eng. Sci. 21 (1979)

403–409.
[4] V. Lepiller, A. Goharzadeh, A. Prigent, I. Mutabazi, Weak temperature gradient effect on the stability of the circular Couette flow, Eur. Phys. J. B 61 (2008) 445–455.
[5] M. Ali, P.D. Weidman, On the stability of circular Couette flow with radial heating, J. Fluid Mech. 220 (1990) 53–84.
[6] J.C. Chen, J.Y. Kuo, The linear stability of steady circular Couette flow with a small radial temperature gradient, Phys. Fluids A 2 (9) (1990) 1585–1592.
[7] K.S. Ball, B. Farouk, Bifurcation phenomena in Taylor-Couette flow with buoyancy effects, J. Fluid Mech. 197 (1988) 479–501.
[8] J.M. Lopez, F. Marques, M. Avila, Conductive and convective heat transfer in fluid flows between differentially heated and rotating cylinders, Int. J. Heat Mass Transf. 90 (2015) 959–967.
[9] M. Lappa, Rotating Thermal Flows in Natural and Industrial Processes, John Wiley & Sons, London, UK, 2012.
[10] S. Viazzo, S. Poncet, Numerical simulation of the flow stability in a high aspect ratio Taylor–Couette system submitted to a radial temperature gradient, Comput. Fluids 101 (2014) 15–26.
[11] R. Guillerm, PhD thesis, Université du Havre, France, 2010.
[12] S. Vedantam, J.B. Joshi, Annular centrifugal contactors—a review, Chem. Eng. J. 84 (A7) (2006) 522–542.
[13] S.T. Wereley, R.M. Lueptow, Inertial particle motion in a Taylor Couette rotating filter, Phys. Fluids 11 (1999) 325–333.
[14] M. Nemri, E. Climent, S. Charton, J.Y. Lanoe, D. Ode, Experimental and numerical investigation on mixing and axial dispersion in Taylor-Couette flow patterns, Chem. Eng. Res. Des. 91 (12) (2013) 2346–2354.
[15] J.S. Olfert, K.S.J. Reavell, M.G. Rushton, N. Collings, The experimental transfer function of the Couette centrifugal particle mass analyzer, J. Aerosol Sci. 37 (2006) 1840–1852.
[16] K. Ehara, C. Hagwood, K.J. Coakley, Novel method to classify aerosol particles according to their mass-to-charge ratio-Aerosol particle mass analyzer, J. Aerosol Sci. 27 (1996) 217–234.
[17] J. Qiao, R. Deng, C.H. Wang, Particle motion in a Taylor vortex, Int. J. Multiphase Flow 77 (2015) 120–130.
[18] S.P. Bhattacharya, Apparent emittance of non-isothermal particulate deposits, Int. Comm. Heat Mass Transf. 26 (6) (1999) 771–780.
[19] M.V. Majji, J.F. Morris, Inertial migration of particles in Taylor-Couette flows, Phys. Fluids 30 (2018) 033303.
[20] D. Coles, Transition in circular Couette flow, J. Fluid Mech. 21 (1965) 385–425.
[21] P.M. Eagles, On the torque of wavy vortices, J. Fluid Mech. 62 (1974) 1–9.
[22] R.C. DiPrima, H.L. Swinney, Instabilities and Transition in Flow between Concentric Rotating Cylinders, Springer-Verlagn, Berlin, 1981, pp. 139–180.
[23] C.D. Andereck, S.S. Liu, H.L. Swinney, Flow regimes in a circular Couette system with independently rotating cylinders, J. Fluid Mech. 164 (1986) 155–183.
[24] D.D. Gray, A. Giorgini, The validity of the Boussinesq approximation for liquids and gases, Int. J. Heat Mass Transf. 19 (5) (1976) 545–551.
[25] ANSYS Fluent, Fluent 14.5 Users Guide, Lebanon, USA (2012).
[26] S.V. Patankar, Numerical Heat Transfer and Fluid Flow, Taylor & Francis, CRC Press, USA, 1980.
[27] M. Rouizi, K. Slamani, Master Dissertation, Faculty of Physics, USTHB, Algeria, 2015.
[28] K.T. Coughlin, P.S. Marcus, A modulated waves in Taylor-Couette flow Part 1. Analysis, J. Fluid Mech. 234 (1992) 1–18.
[29] E.L. Koschmieder, Turbulent Taylor vortex flow, J. Fluid Mech. 93 (3) (1979) 615–627.
[30] M.K. Akbar, M. Rahman, S.M. Ghiaasiaan, Particle transport in a small square enclosure in laminar natural convection, J. Aerosol Sci. 40 (9) (2009) 747–761.
[31] A. Mehel, A. Tanière, B. Oesterlé, J.R. Fontaine, The influence of an anisotropic Langevin dispersion model on the prediction of micro- and nanoparticle deposition in wall-bounded turbulent flows, J. Aerosol Sci. 41 (2010) 729–744.
[32] S.A. Morsi, A.J. Alexander, An investigation of particle trajectories in two-phase flow systems, J. Fluid Mech. 55 (2) (1972) 193–208.
[33] A. Dehbi, J. Kalilainen, T. Lind, A. Auvinen, A large eddy simulation of turbulent particle-laden flow inside a cubical differentially heated cavity, J. Aerosol Sci. 103 (2017) 67–82.
[34] J. Lataste, D. Huilier, H. Burnage, J. Bedna, On the shear lift force acting on heavy particles in a turbulent boundary layer, Atmos. Environ. 34 (2000) 3963–3971.
[35] A. Dehbi, CDF4NRS, (2006), pp. 703–720 unpublished.
[36] H. Ounis, G. Ahmadi, J.B. McLaughlin, Brownian diffusion of submicrometer particles in the viscous sublayer, J. Colloid Interface Sci. 43 (1) (1991) 266–277.